SAND2020-8910J

Influence of Nanoarchitecture on Charge Donation and Electrical Transport Properties in $[(SnSe)_{1+\delta}][TiSe_2]_q$ Heterostructures.

Danielle M. Hamann, [†] Dylan Bardgett,[†] Sage R. Bauers,[†,⊥] Thomas W. Kasel, [†] Austin M. Mroz,[†] Christopher H. Hendon[†], Douglas L. Medlin,[‖] David C. Johnson.[*,†]

[†]*Department of Chemistry and Materials Science Institute, University of Oregon, Eugene, Oregon 97403, USA*

[‖] *Sandia National Laboratories, Livermore, California 94551, USA*

ABSTRACT: A series of $[(SnSe)_{1+\delta}][TiSe_2]_q$ heterostructures with systematic changes in the number of $TiSe_2$ layers in the repeating unit were synthesized and both the structure and electronic transport properties were characterized. The *c*-axis lattice parameter increased linearly as *q* increased and the slope was consistent with the thickness of a $TiSe_2$ layer. In-plane lattice constants for SnSe and $TiSe_2$ were independent of *q*. Temperature dependent resistivity and Hall coefficient data varied systematically as *q* was increased. The low temperature electrical data was modeled assuming only electrons were involved, and the data was fit to a variable range hopping mechanism. The number of carriers involved in this low temperature transport decreased as *q* increased, indicating that approximately $1/10^{th}$ of an electron per SnSe bilayer was transferred to the $TiSe_2$. Calculations also indicated there was charge donation from the SnSe layer to the $TiSe_2$ layer, resulting in an ionic bond between layers which aided in stabilizing the heterostructures. The charge donation created a $TiSe_2$-SnSe-$TiSe_2$ block with properties distinct from the constituent bulk properties. At high temperatures in large *q* samples, the transport data required holes to be activated across a band gap to be successfully modeled. This high temperature transport scales with the number of $TiSe_2$ layers that are not adjacent to SnSe. Using a consistent model across all of the samples significantly constrained the adjustable parameters. The charge transfer between the two constituents results in the stabilization of the heterostructure by an ionic interaction and the formation of a conducting $TiSe_2$-SnSe-$TiSe_2$ block. This is consistent with prior reports, where interactions between 2D layers and their surroundings (i.e. adjacent layers, substrate, or atmosphere) have been shown to strongly influence properties.

While the ability to isolate graphene and other 2D materials has been known since the 1970's, the discovery of an easy optical method to determine the thickness of these thin materials has facilitated an explosion of research activity.[1] Researchers have discovered a number of unusual emergent properties, especially at the monolayer limit, including the conversion of indirect to direct band gaps,[2,3] the observation of the fractional quantum Hall effect,[4] the realization of Hofstadter's butterfly,[5–7] and advances in valleytronics.[8] Researchers also discovered that "artificial" materials created by stacking different 2D layers in designed sequences have emergent properties and provide many experimental parameters (identity, properties, thickness, and sequence of layers) that can be used to modify and manipulate these properties.[9–12] The interaction between a 2D layer and a substrate or a neighboring 2D layers in heterostructures has been found to strongly impact the emergent electronic properties.[13,14] The atomically flat interfaces between adjacent surfaces provides a large area where the orbitals extending from each layer overlap and interact, resulting in a significant renormalization of the electronic states. Due to the easy cleaving of the bulk materials along these crystal planes, the interactions between the layers have typically been described as weak van der Waals interactions, but the substrate dependent properties suggest stronger interactions are present. Understanding the interaction between layers and the impact of these interactions on the near Fermi energy electronic structure is critical to understand the evolution of emergent properties – a critical step in designing heterostructures for next generation devices.

There is significant evidence indicating the common assumption of weak van der Waals bonding between layers in a heterostructure is incorrect. Perhaps, the strongest piece of evidence for stronger interactions between layers in a heterostructure is the thermodynamic stability of the misfit layer compounds, compounds which contain alternating bilayers of a rock salt structure and a monolayer or bilayer of a transition metal dichalcogenide. These compounds are formed via direct reaction of the elements, such as Ti, Se, and Sn, at high temperatures for long time periods.[15] The literature describes the bonding between the layers in these compounds as weak when the cation in the rock salt layer is divalent.[16–18] For these compounds to be thermodynamically stable, however, the bonding between the rock salt structured bilayer and the dichalcogenide layer must be stronger than the sum of the ionic interaction within the bulk rock salt structure and the bonding between layers in the bulk dichalcogenide. A significant interaction between the layers of a heterostructure that is often ignored is charge transfer. Since the chemical potential and dielectric constants of the various constituent layers will be dissimilar, the spatial extent, energies, and occupancy of these wavefunctions will be different in the heterostructure compared to their isolated layers. The resulting charge transfer, a fraction of an electron per formula unit of the constituents, can create a

Sandia National Laboratories is a multimission laboratory managed and operated by National Technology & Engineering Solutions of Sandia, LLC, a wholly owned subsidiary of Honeywell International Inc., for the U.S. Department of Energy's National Nuclear Security Administration under contract DE-NA0003525.

strong "ionic bond" across the interface that stabilizes these compounds.[19] This charge transfer can have a dramatic effect on properties, such as emergent superconductivity of $(SnSe)_{1.18}(TiSe_2)_2$.[15]

In this paper, a series of $[(SnSe)_{1+\delta}][TiSe_2]_q$ heterostructures are synthesized to quantify the amount of charge transfer and probe the importance of charge transfer on the evolution of electrical properties as a function of layer thickness. This system was chosen because the electrical properties of $TiSe_2$ and misfit compounds containing $TiSe_2$ layers are well studied and known to be very sensitive to variations in carrier concentration, specific dopants, defect concentrations, and constituent structures.[15,20–24] $TiSe_2$ has been reported to have a charge density wave, to be a heavily doped semiconductor, and is theoretically calculated to be a semiconductor with a small band gap if made defect free.[20,25–27] SnSe has been reported to be a semiconductor, a promising thermoelectric material, and a topological crystalline material.[28–30] The 1-1 misfit compound has regions of rotational disorder and is a normal metal, while the 1-2 misfit layer compound is superconducting.[15,23,31] In the $[(SnSe)_{1+\delta}]_m[TiSe_2]_1$ homologous series of compounds an unusual change in electronic properties were reported.[24] Here, we prepared and structurally characterized the q = 1,2,3,4, 6, 8, 11 and 15 heterostructures, which all contain a single SnSe layer separated by q layers of $TiSe_2$. Though varying from their bulk counterparts, the constituent crystal structures do not change with nanoarchitecture. The electrical properties systematically evolve as q increases. The changes were successfully modeled based on a $[(SnSe)_{1+\delta}][TiSe_2]_2$ conducting unit that becomes increasingly isolated by $TiSe_2$ layers as q becomes larger. As the number of $TiSe_2$ layers increase the average carrier concentration decreases, and there is increasing localization of the carriers in the $[(SnSe)_{1+\delta}][TiSe_2]_2$ at low temperatures consistent with Anderson localization. In heterostructures with large q values, additional carriers (electrons and holes) are created by thermal excitation at higher temperatures. Density functional theory (DFT) calculations and the modeling of electrical data both indicate charge transfer of approximately 0.1 electron per SnSe to $TiSe_2$. Quantifying the charge transfer between layers and understanding how it changes with nanoarchitecture is important for future design of thin film materials with targeted properties.

METHODS AND MATERIALS

Samples were prepared via the MER method as described previously by Atkins and coworkers.[32,33] Elemental layers were deposited onto Si with a native SiO_2 layer and quartz substrate for structural and electrical characterization, respectively. Titanium and tin (Alfa Aeser, 99.99% and 99.98%, respectively) were deposited using electron beam guns while selenium (Alfa Aeser, 99.999%) was deposited using a Knudson effusion cell. Quartz crystal microbalances, located between the source and the substrate, were used to monitor the deposition rate and thickness of each element. Custom software which communicated with the crystals and controlled the pneumatic shutters, assembled the precursor with the designed architecture and number of atoms per elemental layer calculated to produce the targeted product.[34]

Samples were annealed on a hotplate at 350 °C for 30 minutes in a nitrogen atmosphere with less than 1 ppm oxygen. This temperature was determined in a previous study of $[(SnSe)_{1.2}]_1[TiSe_2]_1$ samples and assumed to be the optimal annealing temperature for these $[(SnSe)_{1+\delta}]_1[TiSe_2]_q$ heterostructures.[31] The annealed structures were determined via x-ray diffraction (XRD) using Cu-Kα radiation (λ = 0.15418 nm). Total film and repeating unit (c-axis lattice parameter) thicknesses were gathered from low angle x-ray reflectivity (XRR) and specular diffraction data, respectively. The reflectivity and specular diffraction data were collected on a Bruker D8-discover diffractometer using a locked couple scan type and (θ-2θ) ranges of 0-10° and 5-65° respectively. The in-plane diffraction scans were collected using a Rigaku Smartlab diffractometer with a (θ-2θ) range of 15-110°.

Ultrathin cross-sections were prepared using a FEI Helios Nanolab 600i focused ion beam scanning electron microscope (FIB-SEM) for electron microscopy investigations. As the lamellae approached electron transparency, low energy 2kV milling was used to avoid damaging the crystallinity of the sample while thinning the sample to the targeted thickness. The prepared samples were imaged in high angle annular dark field scanning transmission electron microscopy (HAADF-STEM) mode at 300kV using a Thermofisher Themis TEM located at Sandia National Laboratory in Livermore, CA.

Temperature-dependent transport measurements were collected on a home-built measurement system that uses a closed-cycle helium cryostat to obtain low temperatures. Resistivity measurements were conducted using the van der Pauw technique. Films were deposited onto a masked quartz substrate to create 1 cm x 1 cm samples with a cross-arm geometry. Indium contacts were pressed onto each of the four points of the cross. Resistivity measurements were taken periodically at temperatures ranging from 20 to 295 K. Hall measurements were done with magnetic fields ranging from 0 to 16 kG also using the van der Pauw technique. At 4 kG increments, a constant current of 0.100 A was sequentially applied to each of the four lead configurations. The Hall Coefficient was determined from the slope of a linear fit of the Hall voltage as a function of magnetic field. Seebeck measurements were performed on a rectangular sample deposited onto a quartz substrate. One end of the sample was cooled, and the temperature difference measured using independent thermocouples. The voltage difference between either end of the sample was measured and divided by the temperature difference to obtain the Seebeck coefficient.

Computational models of bulk SnSe and $TiSe_2$ were prepared from the computationally ready structures from the Materials Project.[35] Prior to generation of slab and heterojunction models, bulk structures were geometrically optimized. All calculations utilized the PBEsol functional[36,37] with Tkatchenko-Scheffler dispersion corrections[38] and a scaling factor of 0.94 alongside a projector-augmented-wave (PAW) basis[39] and a 500 eV plane-wave cutoff as implemented in the Vienna *ab initio* Simulation Package (VASP).[40–43] All structures were considered geometrically optimized when forces were below 0.005 eV/Å^2 and electronically optimized when the total energy was below 10^{-6} eV. A 10 x 10 x 4 Γ-centered k-grid were used for both bulk SnSe and bulk $TiSe_2$. Once bulk models were geometrically optimized, slab models were generated containing 7 layers and ~20 Å of vacuum space with a Γ-centered k-mesh of 10 x 10 x 1 for both SnSe and $TiSe_2$. Density of States plots of slab models were calculated from a minimized wave function using the same electronic convergence criteria as above and Gaussian smearing with σ = 0.3 eV with

a 10 x 10 x 1 and a 6 x 6 x 1 Γ-centered k-grid for SnSe and $TiSe_2$, respectively. The valence band maximum eigenvalue was aligned to vacuum utilizing the MacroDensity code.[44,45] While a previous report on the SnSe-$TiSe_2$ heterojunction utilized an island-based modeling approach,[23] here we elected to utilize supercell expansions of bulk models to maintain the *ab* plane connectivity as to not artificially confine SnSe. This was done by first generating a 6 x 7 x 2 supercell of $TiSe_2$ followed by removal of one of the two $TiSe_2$ sheets to create a cavity for SnSe insertion. SnSe was expanded to a 5 x 6 x 1 supercell and a single layer was inserted into the $TiSe_2$ cavity. The SnSe layer was subsequently rotated about the normal of the *ab* plane by hand to minimize lattice mismatch. Following rotation excess atoms were removed. The resulting heterojunction was geometrically minimized using the criteria above in a spin polarized scheme with a 2 x 2 x 2 Γ-centered k-grid. After geometric optimization, Bader charge analysis was performed on both the heterojunction and bulk models using the Bader code and the charge density was sampled with 150% of the default resolution in all directions.[46–48]

RESULTS AND DISCUSSION

A series of $[(SnSe)_{1+\delta}]_1[TiSe_2]_q$ heterostructures with an increasing number of $TiSe_2$ layers per repeat unit ($1 \le q \le 15$) were prepared from precursors with composition profiles designed to mimic the desired final product. Each precursor was made by depositing elemental layers in a repeating sequence containing a single Sn|Se bilayer and q Ti|Se bilayers. The deposition parameters for the Sn|Se bilayer were adjusted to obtain a one to one atomic ratio of Sn to Se and the required number of atoms such that two 001 planes of rock salt structured SnSe formed from the deposited bilayers when annealed. The deposition parameters for the Ti|Se bilayer were adjusted to obtain a one to two ratio of Ti to Se and a thickness such that a single $TiSe_2$ layer with a CdI_2 structure formed upon annealing. Heterostructures with q = 1, 2, 3, 4, 6, 8, 11, and 15 were targeted by changing the number of Ti|Se bilayers within the repeating unit. The Sn|Se + q[Ti|Se] sequence of layers was repeated 41, 28, 21, 17, 12, 9, 7, and 5 times, respectively, to form precursor films that were approximately 50 nm thick. Annealing at 350°C for 30 minutes converted the designed precursors into the targeted heterostructures, as reported previously for $[(SnSe)_{1+\delta}]_1[TiSe_2]_1$ and $[(SnSe)_{1+\delta}]_m[TiSe_2]_1$ compounds.[24,31]

Figure 1 contains X-ray reflectivity (XRR) patterns of the annealed q = 1, 2, 4, and 6 samples. The patterns contain Kiessig fringes from the interference between the front and the back of the samples and Bragg reflections from the repeating layer sequence. The angle of the first order Bragg reflection systematically decreases as the number of $TiSe_2$ layers increases, consistent with an increasing c-axis lattice parameter. The q = 1, 2, 4, and 6 compounds have 38, 24, 14, and 10 Kiessig fringes between Bragg reflections respectively, indicating the total thickness contains 40, 26, 16, and 12-unit cells in the final product. The number of unit cells in the q = 6 sample matches the number of layers that were deposited in the precursor. The number of unit cells for the q = 1 and q = 4 samples are one less than deposited in the precursor. For the q = 2, there are two fewer unit cells in the annealed sample than deposited in the precursor. The variations in the XRR patterns demonstrating the change in the total number of layers can be observed in figure S1. The decrease in the number of unit cells relative to the number of layers deposited in the precursor for these samples results from deviation in the amount of material deposited compared to the target amount of material needed in each repeating unit, the reaction of the first layer(s) with the substrate, and/or surface oxidation of the film during annealing. The angle where the Kiessig fringes disappear is related to the roughness of the films via the Parratt equation.[49] Most of the fringes can no longer be resolved at ~ 6° degrees 2θ for all of the samples, indicating a roughness less than ~ 0.4 nm. The presence of Bragg reflections in the XRR patterns of the annealed samples parallels those observed in the as-deposited samples indicates that the nanoarchitecture of the precursors are preserved as the desired heterostructures self-assemble (Figure S1).

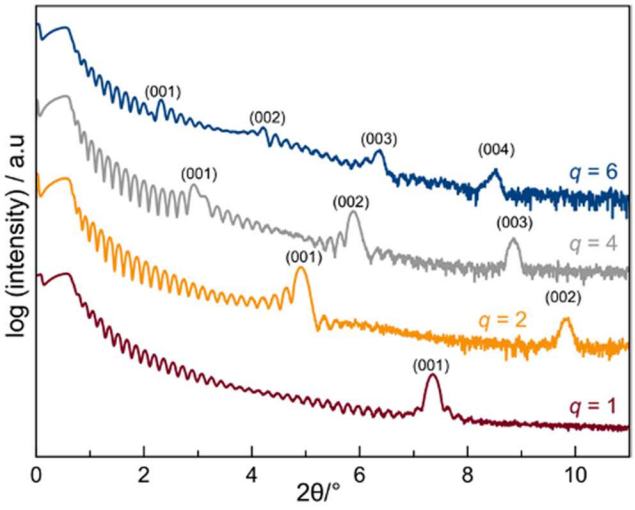

FIGURE 1. XRR patterns of representative $[(SnSe)_{1+\delta}][TiSe_2]_q$ heterostructures after low temperature annealing. The (00*l*) Bragg reflections are indexed and are different from the low intensity maxima between the Bragg reflections known as Kiessig fringes that are due to the finite thickness of the films.

Specular X-ray diffraction scans were collected on each of the $[(SnSe)_{1+\delta}]_1[TiSe_2]_q$ heterostructures and are shown in Figure 2. The intensity maxima in each pattern can all be indexed as (00*l*) reflections, indicating that the heterostructures are crystallographically aligned to the substrate. With increasing q, the spacing between observed Bragg reflections decreases as the c-axis lattice parameter increases. The intensities of most reflections diminish as q increases except for the reflections at approximately 14°, 30°, and 62° 2θ, which become more intense. More of the Fourier terms are needed to describe the structure as the number of ~ 0.6 nm thick $TiSe_2$ layers is increased. The calculated c - axis lattice parameters for the $[(SnSe)_{1+\delta}]_1[TiSe_2]_q$ compounds are given in Table 1. The c - axis lattice parameter of $[(SnSe)_{1.2}]_1[TiSe_2]_1$ is 1.204(1) nm, which is in good agreement with that reported previously for similar compounds.[24,31] The c - axis lattice parameter increases linearly as q increases, with a slope of 0.602(1) nm per $TiSe_2$ layer. This thickness increase per $TiSe_2$ bilayer is consistent with values reported for $[(PbSe)_{1+\delta}]_1[TiSe_2]_q$ compounds.[50–52] The change per $TiSe_2$ layer is also consistent with the c - axis lattice parameter of 1T-$TiSe_2$ (0.6004 nm).[53] Extrapolating the c-axis lattice parameter to q = 0 yields an intercept of 0.600(8) nm, which corresponds to the thickness of the SnSe bilayer and the associated incommensurate interface thickness between the different structures. This thickness is larger than

both the bulk SnSe c - axis lattice parameter of 0.5751(1) nm[54] and the change in c - axis lattice parameter as the SnSe constituent is increased in thickness while the TSe_2 thickness is kept constant in $[(SnSe)_{1+\delta}]_q[TSe_2]_q$ (T = Ti, V, Nb or Ta) heterostructures (0.5775 nm – 0.5806 nm).[24,32,55–57] The added thickness due to the interfaces on either side of SnSe is also similar to the difference between the extrapolated $TiSe_2$ trilayer thickness in the series $[(SnSe)_{1+\delta}]_m[TiSe_2]_1$ relative to the thickness of a $TiSe_2$ layer in 1T -$TiSe_2$.[24] The added thickness is probably due to the structural mismatch at the incommensurate interface between SnSe and $TiSe_2$.

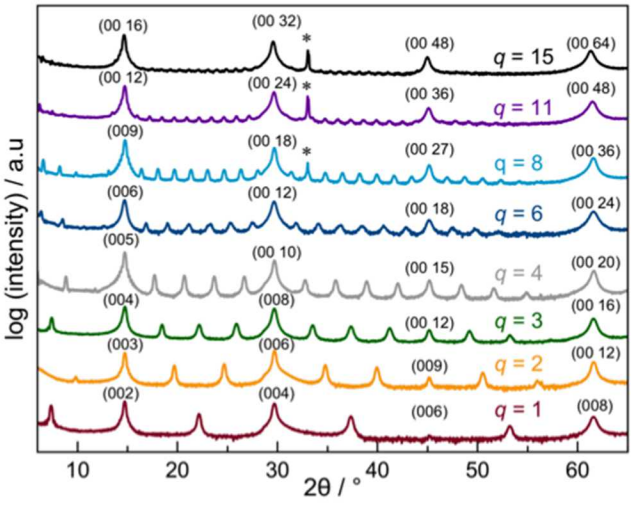

FIGURE 2. Specular diffraction patterns of the $[(SnSe)_{1+\delta}][TiSe_2]_q$ heterostructures. All reflections can be indexed as (00l) Bragg reflections and indices for select reflections are indicated in the pattern. The asterisk marks a Si reflection from the substrate present in particular patterns.

In-plane diffraction was collected to provide information about the a-b- plane crystal structures of the two constituents. All reflections in these scans can be indexed as (hk0) reflections of either a hexagonal or a rectangular unit cell. The intensity of the rectangular unit cell decreases and that of the hexagonal cell increases as q increases. This indicates that the rectangular unit cell is from the SnSe constituent and the hexagonal unit cell is from the $TiSe_2$ constituent. The position of the reflections remains approximately the same for all q values indicating that the in-plane structures of the two constituents do not changing significantly with increasing $TiSe_2$ thickness.

The in-plane lattice parameters for each heterostructures are summarized in Table 1. The a-axis lattice parameter for the $TiSe_2$ constituent varies only slightly as q is increased, with an average value of 0.356(1) nm. This agrees with values previously reported for $TiSe_2$ in both $[(SnSe)_{1+\delta}]_1[TiSe_2]_1$ and $[(SnSe)_{1+\delta}]_m[TiSe_2]_1$,[23,24] as well as other $TiSe_2$ containing heterostructures.[58–63] Bulk $TiSe_2$ has an a - axis lattice parameter of 0.354 nm, which is slightly smaller than the values found in Table 1, reflecting the interaction with the SnSe layer. The SnSe rectangular basal plane unit cell does not change drastically as the thickness of the $TISe_2$ constituent is increased. This is not surprising, as the SnSe layer has the same environment, with $TiSe_2$ interfaces present on both sides of the single SnSe layer, in all of the heterostructures. The average lattice parameters for the SnSe basal plane summarized in Table 1 are 0.596(1) nm and 0.610(2) nm for the a - axis and b - axis lattice parameters, respectively. These are consistent with the values of 0.597(1) nm and 0.610(1) nm previously reported for the $[(SnSe)_{1+\delta}]_1[TiSe_2]_1$ heterostucture.[23,24] The in-plane lattice parameters of SnSe can vary considerably in a heterostructure depending on the dichalcogenide with which it is layered.[64] The lattice parameters reflect the interactions between SnSe and the dichalcogenide, demonstrating the resulting tradeoffs in surface and volume free energy. The basal plane areas of SnSe and $TiSe_2$ remain relatively constant as q is increased, resulting in an average misfit parameter ($1+\delta$) of 1.207(3) (Table 1). This misfit parameter is similar to what was previously reported for $[(SnSe)_{1+\delta}]_1[TiSe_2]_1$ and $[(SnSe)_{1+\delta}]_m[TiSe_2]_1$.[23,24,31]

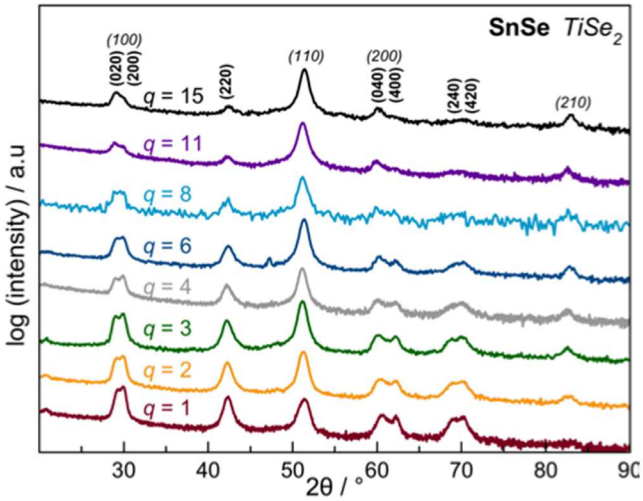

FIGURE 3. In-plane diffraction patterns of $[(SnSe)_{1+\delta}][TiSe_2]_q$ heterostructures. All reflections can be indexed to (hk0) planes of either $TiSe_2$ or distorted SnSe, with the relative intensities of $TiSe_2$ reflections increasing with increasing q.

HAADF-STEM was collected to provide local information about the heterostructures including layer stacking arrangement, constituent structures, extent of rotational disorder between constituent layers, and amount of disproportionation. Representative HAADF-STEM images of $[(SnSe)_{1+\delta}]_1[TiSe_2]_q$, with q = 3, 4 and 8, spanning the entire film thickness are shown in Figure 4. The two different constituent layers are distinguished by their z contrast, with SnSe layers appearing brighter and $TiSe_2$ layers appearing darker. In the SnSe layers the Sn atoms are brighter than the Se atoms. In all images the targeted layering scheme is observed, indicating that the desired heterostructures were formed. Some damage from the focused ion beam sample preparation is visible, and the image for q = 8 has regions where the SnSe bilayer is missing. To further probe the global layering of the heterostructures Fast Fourier transforms (FFT), Figure 4, were taken from the representative HAADF-STEM images. The expected Fourier components for each of the targeted compounds are observed and the spacing between the Fourier components is consistent with the period measured in the specular diffraction pattern. The full thickness HAADF-STEM images and their FFT indicate that the desired layering scheme makes up the majority of the films, which is consistent with the diffraction data discussed previously.

To probe the layer arrangement and zone axis stacking a representative area from the $[(SnSe)_{1+\delta}]_1[TiSe_2]_4$ sample is magnified and shown in Figure 4g. In this image, various zone

TABLE 1. Lattice and misfit parameters for the $[(SnSe)_{1+\delta}]_1[TiSe_2]_q$ heterostructures determined from x-ray diffraction patterns.

q	$[(SnSe)_{1+\delta}][TiSe_2]_q$ *c* – axis lattice parameter / nm	SnSe *a*–axis lattice parameter / nm	SnSe *b*–axis lattice parameter / nm	$TiSe_2$ *a*–axis lattice parameter / nm	1 + δ
1	1.204 (1)	0.597 (1)	0.609 (1)	0.355 (1)	1.202 (1)
2	1.805 (1)	0.597 (1)	0.605 (1)	0.355 (1)	1.210 (1)
3	2.408 (1)	0.597 (1)	0.612 (1)	0.357 (1)	1.206 (1)
4	3.001 (1)	0.598 (1)	0.611 (1)	0.357 (1)	1.207 (1)
6	4.212 (1)	0.595 (1)	0.611 (1)	0.356 (1)	1.207 (1)
8	5.418 (1)	0.595 (1)	0.613 (1)	0.356 (1)	1.203 (1)
11	7.231 (3)	0.597 (1)	0.610 (1)	0.357 (1)	1.209 (1)
15	9.665 (3)	0.595 (1)	0.607 (5)	0.355 (1)	1.210 (1)

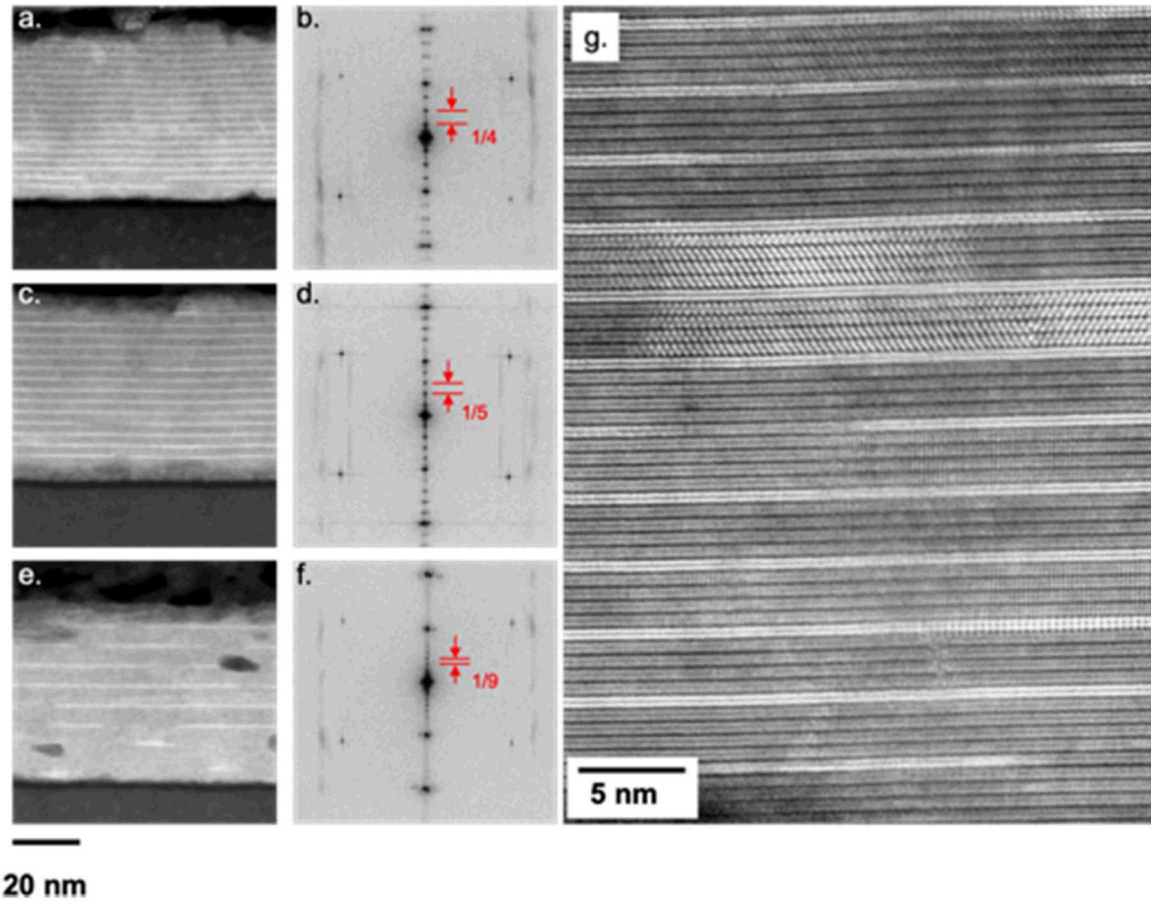

FIGURE 4. HAADF-STEM images and FFT's of the $[(SnSe)_{1+\delta}]_1[TiSe_2]_3$ (a and b), $[(SnSe)_{1+\delta}]_1[TiSe_2]_4$ (c and d), and $[(SnSe)_{1+\delta}]_1[TiSe_2]_8$ (e and f) respectively, and a higher magnification HAADF-STEM image of a region of the $[(SnSe)_{1+\delta}]_1[TiSe_2]_4$ sample (g).

axis and rotations off zone axis can be observed for both constituent layers. This demonstrates the rotational disorder that occurs in the *a*-*b*-plane of the heterostructures. For SnSe the (100) and (110) zones axes are observed, while for $TiSe_2$ the (100) and (110) zone axes are present. Various layering defects are present in the film, but the majority of the area imaged is that of the targeted layering sequence. For example, the bottom SnSe layer in Figure 4g stops while a $TiSe_2$ continues from that space. In the thicker block of $TiSe_2$ there are some unique stacking sequences where there is either

twinning of the $TiSe_2$ layers or places where two different nucleation sites grew together. These layering defects and stacking sequences perhaps provide an opportunity to understand how the precursors self-assemble into the $[(SnSe)_{1+\delta}]_1[TiSe_2]_q$ compounds, however a more thorough investigation is required.

Room temperature Seebeck coefficients collected from the $[(SnSe)_{1+\delta}]_1[TiSe_2]_q$ heterostructures (Figure 5a.) are all negative, suggesting that electrons are the majority carrier. The magnitude of the Seebeck coefficient becomes systematically larger with increasing q indicating that the carrier concentration decreases as the number of $TiSe_2$ layers is increased.[65,66] Koumoto suggested that charge carriers in $[SnSe]_1TiSe_2$ result from the SnSe layer donating electrons to the $TiSe_2$ layer, which dominate the conduction.[16] If the amount of charge donated by the SnSe layer is constant, then the average electron concentration in the $TiSe_2$ layers would decrease as q increases, which is consistent with the data and prior reports of $(MX)_1(TiX_2)$ (M = Pb or Sn and X = S or Se) compounds.[51,52,65] The q- dependency of the Seebeck coefficient, however, has a much steeper negative slope for the $q \leq 3$ heterostructures than for $q \geq 3$ heterostructures, suggesting that there are two regimes dominated by different phenomena.

Variable temperature resistivity data collected from $[(SnSe)_{1+\delta}]_1[TiSe_2]_q$ heterostructures are shown in Figure 5c and 5d. The temperature-dependent resistivity generally increases with more $TiSe_2$ layers present in the repeating unit (the $q = 6$ and 15 samples are exceptions). Samples $q = 6$ and $q = 15$ deviate from the trend, presumably due to different defect concentrations impacting carrier concentrations and/or mobility values. All samples have resistivity upturns as temperature is lowered, with the temperature where the upturn begins increasing as q gets larger. For samples with the largest number of $TiSe_2$ layers in the repeating unit, the resistivity continually goes up with decreasing temperature over the entire temperature regime. The samples with smaller q have a decrease in the resistivity with decreasing temperature from room temperature. Below a certain sample dependent temperature, the resistivity increases as temperature is decreased. The initial decrease in resistivity for the q = 1, 2, 3, 4, and 6 heterostructures is consistent with decreased electron-phonon scattering with lowering of temperature, as expected for a metal. Overall, the rate of resistivity increase at low temperatures for all of the samples is not as large as would be expected for semiconducting behavior. For samples with more $TiSe_2$ layers in the repeating unit, the upturn in the temperature dependent resistivity is similar to previous reports on $TiSe_2$ where the samples were reported to have low defect concentrations.[20]

To further probe the transport behavior, Hall coefficients were measured for the $[(SnSe)_{1+\delta}]_1[TiSe_2]_q$ heterostructures as a function of temperature (Figure 5b). Each heterostructure exhibits a negative Hall coefficient throughout the entire temperature range, which is consistent with the negative room temperature Seebeck coefficients (Figure 5a). However, it appears as if the samples with $q \geq 8$ will have positive Hall coefficients at temperatures slightly above the range measured (above ~300 K). At low temperatures, the negative Hall coefficient with decreasing temperature suggests that electrons dominate the transport properties in this regime. The increase in the magnitude of the Hall coefficient with decreasing temperature, which systematically increases as q gets larger, implies that the carrier concentration decreases as temperature is decreased, and decreases more in high q heterostructures. The temperature dependence of the samples with larger q values also suggests that there are two different phenomena present, one that dominates at low temperature and one that dominates at high temperatures.

The transport properties of all samples in the low temperature regime suggest that the carrier concentration decreases as temperature declines. As q, the number of $TiSe_2$ layers in the repeating unit gets bigger, both the upturns in resistivity and the systematic increase in the absolute magnitude of the Hall coefficient get larger. The temperature dependence of the resistivity at low temperatures cannot be fit to an exponential for any of the samples (see Figure S1). This suggests that the decrease in resistivity as temperature is increased does not result from excitation across a band gap. A charge or spin density wave would be consistent with a decrease in carriers as temperature is lowered, however we did not find any discontinuities in lattice parameters as a function of temperature. (see Figure S2). Similar non-exponential temperature dependence in resistivity and Hall coefficient data has been seen observed in other materials and attributed to variable range hopping (VRH). VRH is commonly observed in disordered systems and is identified by its characteristic ln resistivity vs $T^{-1/4}$ temperature dependency.[67–72]

The low temperature transport data from all heterostructures was fit with a VRH model assuming that a single band approximation at low temperatures. The resistivity data was fit to equation 1:

$$\rho(T) = \rho_o \exp[(T_M/T)^{1/4}], \qquad \text{(equation 1)}$$

where $\rho(T)$ is the resistivity as a function of temperature, ρ_o is the resistivity when all of the carriers are mobile, T is the temperature, and T_M is a characteristic temperature related to the energy needed for hopping to occur.[70] The temperature dependence of the Hall coefficients was fit to equation 2:

$$R_H = \frac{-1}{|e|\, n(T)} = -\left(\frac{\exp[(\frac{T_M}{T})^{\frac{1}{4}}]}{|e|\, n_0} \right) \qquad \text{(equation 2)}$$

where n(T) is the number of mobile carriers and n_o is the total number of carriers that can become mobile. $n_o = 1/\rho_o e\mu$ where μ is the mobility. These equations fit the transport data below 150 K for all values of q well (Figure 5b, 5c, 5d).

As shown in Figure 6, the fitted n_o values generally decrease as the number of $TiSe_2$ layers in the unit cell increases. The carriers donated by SnSe to adjacent $TiSe_2$ layers ($n_{SnSe \rightarrow TiSe2}$) are diluted by additional $TiSe_2$ layers as q increases. If the amount of charge donated is constant in this family of compounds, an estimate for $n_{SnSe \rightarrow TiSe2}$ would be the value of n_o in the $[(SnSe)_{1+\delta}]_1[TiSe_2]_1$ compound. This value is consistent with previous estimates of the amount of charge donated from SnSe or PbSe layers to $TiSe_2$ layers.[51,52,65] The amount of charge donated is about $^1/_{10}$ of an electron per SnSe bilayer, which suggests that there is a significant electrostatic interaction between the constituent layers that helps to stabilize these compounds. n_o would vary as $n_{SnSe \rightarrow TiSe2}/\, q + 1$, where q is the number of $TiSe_2$ layers in the heterostructures if the amount of charge donated was constant. The calculated values from this simple model consistently underestimate the n_o values derived from the fits to the data, suggesting that the amount of charge donation increases as q increases (see Figure 6). Defects in $TiSe_2$ layers

also become an increasingly important source of potential carriers as q increases. The values of T_M obtained from the fits increase systematically as q increases (see table 2). The increase in T_M values correlates with a decrease in the

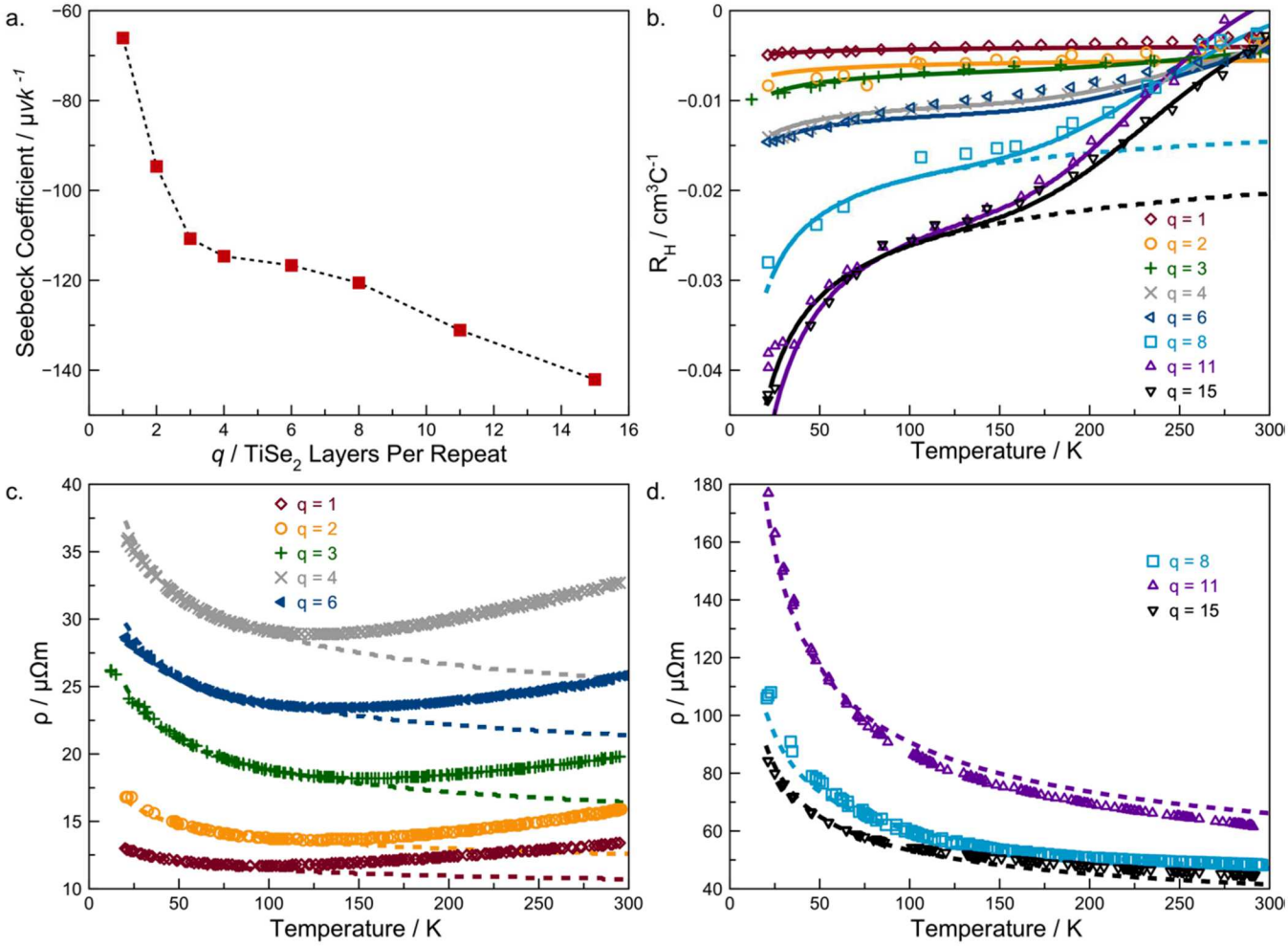

FIGURE 5. Seebeck coefficients for $[(SnSe)_{1+\delta}]_1[TiSe_2]_q$ heterostructures plotted as a function of the number of $TiSe_2$ layers in the unit cell, q (a.). Temperature-dependent Hall coefficients (b.) and resistivity data for the $[(SnSe)_{1+\delta}][TiSe_2]_q$ heterostructures. The resistivity data are plotted on two different resistivity scales (c. q = 1 - 6 and d. q = 8 - 15) so the temperature dependence in samples with thinner $TiSe_2$ layer blocks can be observed. The solid lines in b. are models calculated from a two-carrier model with variable range hopping at low temperatures as discussed in the text which describes the entire temperature regime. The dashed lines in b., c., and d. show the fits to a VRH mechanism, which describes the Hall coefficient and resistivity at low temperatures.

TABLE 2. Parameters obtained for fits of the temperature dependent Hall coefficient and resistivity transport data. Parameters we determined assuming charge transfer from SnSe to $TiSe_2$ results in carriers that are localized at low temperature due to variable range hopping and at high temperatures holes and additional electrons are created due to activation of carrier across a band gap requiring a 2-carrier model. The low temperature parameters were used to fit the VRH model and the 2-carrier model with VRH at low temperatures.

q	μ_h / cm^2 v^{-1} s^{-1}	μ_e / cm^2 v^{-1} s^{-1}		n_i / cm^{-3}		E_a / meV	T_m / K
	High T	High T	Low T	High T	Low T		
1	NA	NA	3.75	NA	1.9×10^{21}	NA	0.5
2	NA	NA	4.4	NA	1.5×10^{21}	NA	2
3	5	1	3.8	3.70×10^{21}	1.55×10^{21}	110	11
4	6	1	3.8	5.92×10^{21}	9.5×10^{20}	107	7
6	6.5	1	5.0	8.46×10^{21}	8.2×10^{20}	107	4
8	5	1	3.1	9.87×10^{21}	9.5×10^{20}	113	120
11	5.5	1	2.85	1.11×10^{22}	9.0×10^{20}	115	300

15	5.4	1	4.9	1.20×10^{22}	6.8×10^{20}	113	120

average carrier concentration, suggesting that decreased screening causes an increase in localization. Edwards and Sienko correlated the behavior of many systems that undergo a metal to non-metal transition,[73] showing that carriers become localized when the product of the carrier concentration and the effective Bohr radius reaches a critical value. The behavior observed here suggests that a metal to non-metal transition is occurring, in part driven by disorder, as carrier concentration is decreased. Further analysis looking at the derivatives of conductivity has been proposed by Mobius to determine the origin of the metal to non-metal transition but requires careful temperature equilibration before transport properties are measured.[74]

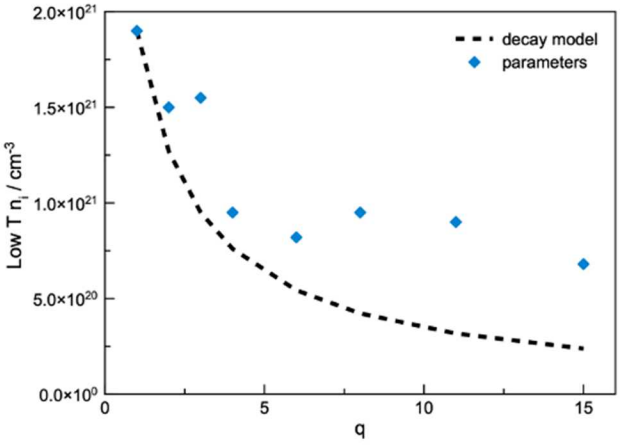

FIGURE 6. The values of the number of carriers that can become mobile for the low temperature activated process, n_o, plotted as a function of the number of $TiSe_2$ layers in the sample. n_o values were obtained by fitting the low temperature transport data using a single band, variable range hopping model. The dashed line assumes that n_o should vary as $n_{SnSe \rightarrow TiSe2} / q + 1$, where q is the number of $TiSe_2$ layers in the heterostructures and use the $n_{SnSe \rightarrow TiSe2}$ obtained from the $[(SnSe)_{1+\delta}]_1[TiSe_2]_1$ compound.

Mobility values were calculated directly from the resistivity and Hall data at low temperatures where electrons dominate the transport behavior. The average mobility values in the low temperature regime are given in Table 2. Values range from 2.85 $cm^2v^{-1}s^{-1}$ to 5.0 $cm^2v^{-1}s^{-1}$ with an average value of 4.0(8) $cm^2v^{-1}s^{-1}$ and do not systematically change as the number of $TiSe_2$ layers is varied. These mobility values are similar to those reported previously for $[(SnSe)_{1+\delta}]_m[TiSe_2]_q$ misfit layer compounds and low compared to values previously reported for bulk and thin film $TiSe_2$.[26,31,75]

The Hall coefficient data above 150 K for samples with a large number of $TiSe_2$ layers in the repeating unit cell suggests that there is another process that results in the activation of additional carriers. Recently, Watson et al. suggested that the electrical properties of $TiSe_2$ are dominated by either electrons or holes depending on the temperature regime. At low temperatures the transport behavior of $TiSe_2$ is dominated by electrons from defects, but above 150 K activation of intrinsic carriers occurs and holes become increasingly important in the transport. The influence of the activated holes becomes more pronounced due to their higher mobility relative to their electron counterparts.[76] We fit our transport data to the two-carrier model suggested by Watson et al., with an additional term for the electrons donated from SnSe to the $TiSe_2$ layers at low temperature:

$$R_H = \frac{[\mu_h{}^2 n_h - \mu_{e(highT)}{}^2 n_{e(highT)} - \mu_{e(lowT)}{}^2 n_{e(lowT)}}{\{|e|[\mu_h n_h + \mu_{e(highT)} n_{e(highT)} + \mu_{e(lowT)} n_{e(lowT)}]^2\}}$$

(equation 3).

In equation 3 μ_h, $\mu_{e(highT)}$ and $\mu_{e(lowT)}$ are the hole and electron mobilities, and n_h, $n_{e(lowT)}$, and $n_{e(lowT)}$ are the hole and electron carrier concentrations, respectively.[76] The mobility values were assumed to be temperature independent. This model is not sensitive to the mobility of the electrons created from the high temperature process because the larger number of electrons from the low temperature process dominate the average electron mobility. We assumed that the mobility values for the holes dominate the high temperature process due to their higher mobility, as suggested by Watson, and set $\mu_{elowT} = 1$ cm^2 v^{-1} s^{-1}. The hole concentration was assumed to come only from activation at high temperatures (equation 4),

$$n_h = n_{i(high\ T)}\ e^{[-Ea/kT]} \quad \text{(equation 4)}.$$

The electron concentration was assumed to be the sum of the low and high temperature carriers (equation 5):

$$n_e = n_{e(low\ T)} + n_{e(high\ T)} \quad \text{(equation 5)}$$

where:

$$n_{e(low\ T)} = n_{i(low\ T)}/\exp[(T/T_M)^{1/4}] \quad \text{(equation 6)}$$

$$n_{e(high\ T)} = n_{i(high\ T)}\ e^{[-Ea/kT]}. \quad \text{(equation 7)}.$$

The fits are not very sensitive to the value of $n_{i(high\ T)}$ due to the small temperature range for which there is data. We set $n_{i(high\ T)}$ to be close to the density of Se atoms in $TiSe_2$ (n_{TiSe2}). Since charge transfer between SnSe and $TiSe_2$ will modify the electronic structure of layers close to the interface, the fraction of bulk-like $TiSe_2$ in each unit cell varies as

$$[(q - x)/(q + 1)] \quad \text{(equation 8)}$$

where q is the number of $TiSe_2$ layers in the unit cell, $q + 1$ is the total number of layers (SnSe + $TiSe_2$) in the unit cell, and x is the number of layers near the interface that do not behave as bulk $TiSe_2$ due to the charge transfer. Therefore,

$$n_{i(high\ T)} = n_{TiSe2}\ [(q - x)/(q + 1)]. \quad \text{(equation 9)}$$

The high temperature carrier concentration, $n_{i(high\ T)}$, calculated with x = 2 gave the most constant values for the hole mobilities and high temperature activation energy (E_a) across all samples. This is reasonable since there are two $TiSe_2$ layers adjacent to SnSe which will be most impacted by the charge donated by SnSe to $TiSe_2$.

The model does reasonably well at fitting the temperature dependence of the Hall coefficients, with the solid lines in Figure 5b demonstrating the result of the fits for each sample. The low temperature fitted values for the low temperature T_M (Table 2), and the low temperature carrier concentration ($n_{i(low\ T)}$) (Figure 6) were used in these fits. The values for the hole mobilities and high temperature activation energy (E_a) are similar for all of the samples. The average activation energy for the high temperature carriers, ~ 0.11(1) eV, is similar to values previously reported for bulk $TiSe_2$.[77] The average hole mobility value, μ_h, is 5.4(1) cm^2 v^{-1} s^{-1}, which

is higher than values previously reported for the $[(SnSe)_{1+\delta}]_m[TiSe_2]_q$ misfit layer compounds[31] and lower than the range reported previously for $TiSe_2$.[26,75] The hole mobility needs to be higher than the mobility of the electrons created by excitation across the gap to reproduce the decreasing absolute value of the Hall coefficient observed as temperature increases.[76]

The resistivity is given by equation 10:

$$\rho\frac{1}{\sigma} = \frac{1}{[|e|(\mu_h n_h + \mu_{e(highT)} n_{e(highT)} + \mu_{e(lowT)} n_{e(lowT)})]} \quad \text{(equation 10)}$$

where μ_h, n_h, μ_e and n_e are defined as described above. The values obtained for the carrier concentration, mobility, activation energy and characteristic hopping energy from fitting the Hall coefficient data to the two-carrier model (table 2) reproduce the low temperature resistivity data reasonable for all of the samples (Figure 5). This suggests that the resistivity can be described by a single carrier model in this temperature range. The agreement at high temperature is not good, as the model underestimates the resistivity. This suggest that the assumption of a temperature independent mobility is not valid.

DFT was used to model the electronic structure of bulk SnSe, $TiSe_2$, the surfaces of each, and a large-scale epitaxial model of the $q = 1$ system to further understand the properties observed in the heterostructures. Following the computational procedure detailed in the materials and methods section, three key properties were obtained; i) the electronic band gaps of both bulk materials, ii) the work functions for slab models thereof, and iii) representative charge densities in both the slab and epitaxial models. Together, these properties provide additional and complimentary insights into the mechanism of charge donation in $[(SnSe)_{1+\delta}]_1[TiSe_2]_q$ heterostructures. The electronic band gaps of bulk SnSe and $TiSe_2$ were computed using the hybrid GGA functional, HSE06,[78] known to perform well for narrow gap semiconductors. As informed by the crystallography, SnSe is modeled as face-centered cubic, whose band gap is predicted to be 0.5 eV. Other crystal polymorphs were also explored, and their band gaps are presented in the Supporting Information Table S1. The workfunction (Φ = 4.3 eV) was recovered using a surface slab model and permits the alignment of the valence band energy, and therefore computational Fermi level, to the vacuum (Figure 7). A seven layer slab was used to sufficiently account for the bulk, as well as its surface, and was aligned using a method previously described.[44] A similar procedure was performed for $TiSe_2$, however, both GGA and hybrid GGA approaches are known to predict bulk metallicity in $TiSe_2$,[79,80] despite experimental evidence for a thermally activated transport mechanism. Indeed, a narrow band gap (200-300 meV) is recovered using a GW approach,[81] but the procedure does not significantly augment the workfunction. Here, the nature of the gap is less important that the workfunction. Hence, $TiSe_2$ is presented as a bulk metal with a workfunction of 5.5 eV (Figure 7). A comparison of these computed workfunctions suggests that spontaneous charge transfer should occur between SnSe and $TiSe_2$, as the valence band of the former lays above the conduction band of the latter.

To test this hypothesis, a lattice matched $[(SnSe)_{1+\delta}]_1[TiSe_2]_1$ model was constructed, minimizing the lattice mismatch by expanding the unit in the a-b plane to a 6 x 7 supercell as shown in Figure 7. A Bader charge analysis[46] was done on bulk SnSe and $TiSe_2$ and the lattice matched $[(SnSe)_{1+\delta}]_1[TiSe_2]_1$ to provides a quantitative estimate of the extent of charge transfer between the materials.

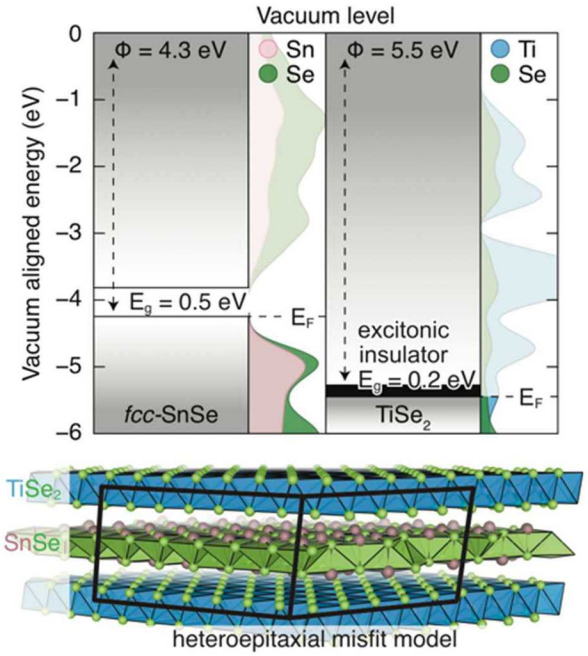

FIGURE 7. Vacuum aligned Density of States for SnSe and $TiSe_2$ slab models. The frontier valence of SnSe is ~1.2 eV above that of $TiSe_2$, indicating that charge transfer from SnSe to $TiSe_2$ would occur at the interface between them.

TABLE 3. Average atomic charge of bulk SnSe, bulk $TiSe_2$, and the average charge transfer between them in the heterojunction.

	Avg. Charge in Bulk / Bohr^{-3}	Avg Charge in Heterostructure / Bohr^{-3}	Avg. Charge Transfer / Bohr^{-3}
Sn	0.777	0.860	0.083
Ti	1.341	1.345	0.004
Se in SnSe	-0.777	-0.729	0.048
Se in $TiSe_2$	-0.671	-0.747	-0.076

In the bulk structures, positive charges are observed on the cations and negative charges are observed on the anions. The smaller negative charge on the Se in $TiSe_2$ reflects the covalent hybridization of the Ti and Se orbitals in this compound. By comparing the charges in the bulk structures with the charges calculated for the lattice matched heterostructure, a charge transfer from SnSe to $TiSe_2$ is observed in the heterostructure (Table 3). The magnitude of the electron transfer from SnSe to $TiSe_2$ is approximately 10%, in excellent agreement with the experimental observation of 1/10th of an electron per formula unit. Interestingly, the added charge in $TiSe_2$ is localized on the Se rather than the Ti, reflecting the extent of covalent character in the bonding of this compound. There is a net "ionic" bond between the layers of SnSe and $TiSe_2$, with higher electron density in the lone pair of the Se atoms in $TiSe_2$ and a positive charge in the SnSe planes. This picture agrees well with the analysis of the

transport properties, which suggests that the two $TiSe_2$ layers adjacent to SnSe have different transport properties than those not adjacent to SnSe. The added charge to the conduction band indicated in the calculation agrees well with the metallic like conductivities observed for the small *q* heterostructures above the hopping temperature. The calculation also provides a basis for the model shown in Figure 7. A calculation of the stabilization energy of the ionic "bond" between the layers is surprisingly high, 3.6 eV, suggesting that this interaction is a key factor in stabilizing the heterostructures. This ionic interaction between layers makes $[(SnSe)_{1+\delta}]_1[TiSe_2]_1$ more stable than a physical mixture of SnSe and $TiSe_2$ by ~ 0.09 eV, consistent with the thermodynamic stability of the known misfit layer compound.[15]

CONCLUSIONS

A series of compounds $[(SnSe)_{1+\delta}]_1[TiSe_2]_q$ were prepared and the structural data indicates that the structure of the constituent layers are similar in all of the heterostructures. The electrical properties suggest that charge donation from the SnSe to the $TiSe_2$ layers occurs, resulting in metallic behavior for samples with a low number of $TiSe_2$ layers. The carrier concentration decreases as the number of $TiSe_2$ layers increase. Localization of the carriers occurs at low temperature, with the temperature required to activate the hopping of these carriers increasing as the $TiSe_2$ layer thickness is increased. DFT calculations show that the valence band of SnSe is higher in energy than the conduction band of $TiSe_2$, supporting the experimentally suggested charge transfer from SnSe to $TiSe_2$. The calculations suggest that the charge transfer between the constituents contributes a significant "ionic" stabilization of these heterostructures, which may be the key factor in their kinetic stability. Similar charge transfer effects will be present in all heterostructures to equalize the chemical potential and understanding how they modify properties is necessary for the synthesis of novel materials with designer properties.

ASSOCIATED CONTENT

Supporting Information

The Supporting Information is available free of charge on the ACS Publications website.

X-ray reflectivity patterns of representative heterostructures before and after annealing at 350 C for 30 minutes in an N_2 atmosphere, very low temperature dependent resistivity measurements of representative heterostructures demonstrating the non-exponential behavior with decreasing temperature, temperature dependent in-plane lattice parameters of both constituents demonstrating that the structures do not change as temperature decrease, and DFT calculated electronic band gaps.

AUTHOR INFORMATION

Corresponding Author

* E-mail: davej@uoregon.edu

Present Addresses

⊥Materials Science Center, National Renewable Energy Laboratory, Golden, Colorado 80309, USA

Author Contributions

The manuscript was written through contributions of all authors.

Funding Sources

National Science Foundation grant DMR-1710214 and DMR - 1956403
National Science Foundation Graduate Research Fellowship Program grant - 1309047

Notes

The Authors declare no competing financial interest.

ACKNOWLEDGMENT

This material is based upon work supported by the National Science Foundation Graduate Research Fellowship Program under Grant No. 1309047. The authors acknowledge support from the National Science Foundation under grants DMR-1710214 and DMR-1956403. Sandia National Laboratories is a multimission laboratory managed and operated by National Technology and Engineering Solutions of Sandia, LLC, a wholly owned subsidiary of Honeywell International Inc. for the U.S. Department of Energy's National Nuclear Security Administration under contract DE-NA-0003525. Any opinions, findings, and conclusions or recommendations expressed in this material are those of the author(s) and do not necessarily reflect the views of the National Science Foundation, the Department of Energy, or the United States Government. This work was supported by the University of Oregon Department of Chemistry and Biochemistry. This work benefitted from access to the University of Oregon high performance computer, Talapas. We would like to acknowledge the Center for Advanced Materials Characterization in Oregon (CAMCOR) at the University of Oregon. The authors acknowledge use of beamline 33BM-C at the Advanced Photon Source. The Advanced Photon Source at Argonne National Laboratory is a User Facility un the Office Science and is operated for the Department of Energy office of Science. It is supported by the DOE (contract no. DE-AC02-06CH11257).

ABBREVIATIONS

2D, two-dimensional; DFT, density functional theory; XRD, x-ray diffraction; XRR, x-ray reflectivity; FIB-SEM, focused ion beam scanning electron microscope; HAADF-STEM, High angle annular dark field scanning transmission electron microscopy; VASP, Vienna *ab initio* Simulation; PAW, projector-augmented-wave; VRH, variable range hopping.

REFERENCES

(1) Ni, Z. H.; Wang, H. M.; Kasim, J.; Fan, H. M.; Yu, T.; Wu, Y. H.; Feng, Y. P.; Shen, Z. X. Graphene Thickness Determination Using Reflection and Contrast Spectroscopy. *Nano Lett.* **2007**, *7*, 2758–2763.

(2) Mak, K. F.; Lee, C.; Hone, J.; Shan, J.; Heinz, T. F. Atomically Thin MoS_2: A New Direct-Gap Semiconductor. *Phys. Rev. Lett.* **2010**, *105*.

(3) Tongay, S.; Zhou, J.; Ataca, C.; Lo, K.; Matthews, T. S.; Li, J.; Grossman, J. C.; Wu, J. Thermally Driven Crossover from Indirect toward Direct Bandgap in 2D Semiconductors: $MoSe_2$ versus MoS_2. *Nano Lett.* **2012**, *12*, 5576–5580.

(4) Bolotin, K. I.; Ghahari, F.; Shulman, M. D.; Stormer, H. L.; Kim, P. Observation of the Fractional Quantum Hall Effect in Graphene. *Nature* **2009**, *462*, 196–199.

(5) Dean, C. R.; Wang, L.; Maher, P.; Forsythe, C.; Ghahari, F.; Gao, Y.; Katoch, J.; Ishigami, M.; Moon, P.; Koshino, M.; et al. Hofstadter's Butterfly and the Fractal Quantum Hall Effect in Moiré Superlattices. *Nature* **2013**, *497*, 598–602.

(6) Ponomarenko, L. A.; Gorbachev, R. V.; Yu, G. L.; Elias, D. C.; Jalil, R.; Patel, A. A.; Mishchenko, A.; Mayorov, A. S.; Woods, C. R.; Wallbank, J. R.; et al. Cloning of Dirac Fermions in Graphene Superlattices. *Nature* **2013**, *497*, 594–597.

(7) Hunt, B.; Sanchez-Yamagishi, J. D.; Young, A. F.; Yankowitz, M.; LeRoy, B. J.; Watanabe, K.; Taniguchi, T.; Moon, P.;

Koshino, M.; Jarillo-Herrero, P.; et al. Massive Dirac Fermions and Hofstadter Butterfly in a van Der Waals Heterostructure. *Science.* **2013**, *340*, 1427–1430.

(8) Schaibley, J. R.; Yu, H.; Clark, G.; Rivera, P.; Ross, J. S.; Seyler, K. L.; Yao, W.; Xu, X. Valleytronics in 2D Materials. *Nature Reviews Materials*. Nature Publishing Group August 23, 2016, 1–15.

(9) Geim, A. K.; Grigorieva, I. V. Van Der Waals Heterostructures. *Nature* **2013**, *499*, 419–425.

(10) Novoselov, K. S.; Mishchenko, A.; Carvalho, A.; Castro Neto, A. H. 2D Materials and van Der Waals Heterostructures. *Science.* **2016**, *353*.

(11) Jariwala, D.; Sangwan, V. K.; Lauhon, L. J.; Marks, T. J.; Hersam, M. C. Emerging Device Applications for Semiconducting Two-Dimensional Transition Metal Dichalcogenides. *ACS Nano*. American Chemical Society February 25, 2014, 1102–1120.

(12) Cui, X.; Lee, G. H.; Kim, Y. D.; Arefe, G.; Huang, P. Y.; Lee, C. H.; Chenet, D. A.; Zhang, X.; Wang, L.; Ye, F.; et al. Multi-Terminal Transport Measurements of MoS_2 Using a van Der Waals Heterostructure Device Platform. *Nat. Nanotechnol.* **2015**, *10*, 534–540.

(13) Grubišić Čabo, A.; Miwa, J. A.; Grønborg, S. S.; Riley, J. M.; Johannsen, J. C.; Cacho, C.; Alexander, O.; Chapman, R. T.; Springate, E.; Grioni, M.; et al. Observation of Ultrafast Free Carrier Dynamics in Single Layer MoS_2. *Nano Lett.* **2015**, *15*, 5883–5887.

(14) Wang, Y. Y.; Ni, Z. H.; Yu, T.; Shen, Z. X.; Wang, H. M.; Wu, Y. H.; Chen, W.; Wee, A. T. S. Raman Studies of Monolayer Graphene: The Substrate Effect. *J. Phys. Chem. C* **2008**, *112*, 10637–10640.

(15) Song, Y. J.; Kim, M. J.; Jung, W. G.; Kim, B.-J.; Rhyee, J.-S. Superconducting Properties of the Misfit-Layer Compound $(SnSe)_{1.18}(TiSe_2)_2$. *Phys. status solidi* **2016**, *253*, 1517–1522.

(16) Wan, C.; Wang, Y.; Wang, N.; Koumoto, K. Low-Thermal-Conductivity $(MS)_{1+x}(TiS_2)_2$ (M = Pb, Bi, Sn) Misfit Layer Compounds for Bulk Thermoelectric Materials. *Materials (Basel).* **2010**, *3*, 2606–2617.

(17) Ryu, Y. K.; Frisenda, R.; Castellanos-Gomez, A. Superlattices Based on van Der Waals 2D Materials. *Chem. Commun.* **2019**, *55*, 11498–11510.

(18) Radovsky, G.; Popovitz-Biro, R.; Stroppa, D. G.; Houben, L.; Tenne, R. Nanotubes from Chalcogenide Misfit Compounds: Sn-S and Nb-Pb-S. *Acc. Chem. Res.* **2014**, *47*, 406–416.

(19) Meerschaut, A. Misfit Layer Compounds. *Curr. Opin. Solid State Mater. Sci.* **1996**, *1*, 250–260.

(20) Huang, S. H.; Shu, G. J.; Pai, W. W.; Liu, H. L.; Chou, F. C. Tunable Se Vacancy Defects and the Unconventional Charge Density Wave in 1T-$TiSe_{2-\delta}$. *Phys. Rev. B* **2017**, *95*, 45310.

(21) Levy, F. Electrical Resistivity and Hall Effect in $TiSe_2$ Containing Vanadium Impurities. *J. Phys. C Solid State Phys.* **1979**, *12*, 3725–3732.

(22) Levy, F. The Influence of Impurities on the Electrical Properties of $TiSe_2$ Single Crystals. *J. Phys. C Solid State Phys.* **1980**, *13*, 2901–2912.

(23) Hamann, D. M.; Merrill, D. R.; Bauers, S. R.; Mitchson, G.; Ditto, J.; Rudin, S. P.; Johnson, D. C. Long-Range Order in $[(SnSe)_{1.2}]_1[TiSe_2]_1$ Prepared from Designed Precursors. *Inorg. Chem.* **2017**, *56*, 3499–3505.

(24) Hamann, D. M.; Lygo, A. C.; Esters, M.; Merrill, D. R.; Ditto, J.; Sutherland, D. R.; Bauers, S. R.; Johnson, D. C. Structural Changes as a Function of Thickness in $[(SnSe)_{1+\delta}]_m$ $TiSe_2$ Heterostructures. *ACS Nano* **2018**, *12*, 1285–1295.

(25) Rasch, J.; Stemmler, T.; Müller, B.; Dudy, L.; Manzke, R. 1 T-TiSe 2: Semimetal or Semiconductor? *Phys. Rev. Lett.* **2008**, *237602* (December), 2–5.

(26) Di Salvo, F. J.; Moncton, D. E.; Waszczak, J. V. Electronic Properties and Superlattice Formation in the Semimetal $TiSe_2$. *Phys. Rev. B* **1976**, *14*, 4321–4328.

(27) Fang, C. M.; De Groot, R. A.; Haas, C. *Bulk and Surface Electronic Structure of 1T-TiS_2 and 1T-$TiSe_2$*; 1997.

(28) Zhao, L.-D.; Lo, S.-H.; Zhang, Y.; Sun, H.; Tan, G.; Uher, C.; Wolverton, C.; Dravid, V. P.; Kanatzidis, M. G. Ultralow Thermal Conductivity and High Thermoelectric Figure of Merit in SnSe Crystals. *Nature* **2014**, *508*.

(29) Jin, W.; Vishwanath, S.; Liu, J.; Kong, L.; Lou, R.; Dai, Z.; Sadowski, J. T.; Liu, X.; Lien, H.-H.; Chaney, A.; et al. Electronic Structure of the Metastable Epitaxial Rock-Salt SnSe F111g Topological Crystalline Insulator.

(30) Cui, Z.; Wang, X.; Ding, Y.; Li, M. Exploration Work Function and Optical Properties of Monolayer SnSe Allotropes. *Superlattices Microstruct.* **2018**, *114*, 251–258.

(31) Merrill, D. R.; Moore, D. B.; Ditto, J.; Sutherland, D. R.; Falmbigl, M.; Winkler, M.; Pernau, H.-F.; Johnson, D. C. The Synthesis, Structure, and Electrical Characterization of $(SnSe)_{1.2}TiSe_2$. *Eur. J. Inorg. Chem.* **2015**, *2015*, 83–91.

(32) Atkins, R.; Wilson, J.; Zschack, P.; Grosse, C.; Neumann, W.; Johnson, D. C. Synthesis of $[(SnSe)_{1.15}]_m((TaSe_2)_n$ Ferecrystals: Structurally Tunable Metallic Compounds. *Chem. Mater.* **2012**, *24*, 4594–4599.

(33) Johnson, D. C. Controlled Synthesis of New Compounds Using Modulated Elemental Reactants. *Curr. Opin. Solid State Mater. Sci.* **1998**, *3*, 159–167.

(34) Esters, M. Deposition Software for the Inficon IC6 Deposition Controller https://github.com/marcoesters/deposition_ic6.

(35) Jain, A.; Ong, S. P.; Hautier, G.; Chen, W.; Richards, W. D.; Dacek, S.; Cholia, S.; Gunter, D.; Skinner, D.; Ceder, G.; et al. Commentary: The Materials Project: A Materials Genome Approach to Accelerating Materials Innovation. *APL Mater.* **2013**, *1* (1), 011002.

(36) Perdew, J. P.; Burke, K.; Ernzerhof, M. Generalized Gradient Approximation Made Simple. *Phys. Rev. Lett.* **1996**, *77*, 3865–3868.

(37) Perdew, J. P.; Ruzsinszky, A.; Csonka, G. I.; Vydrov, O. A.; Scuseria, G. E.; Constantin, L. A.; Zhou, X.; Burke, K. Restoring the Density-Gradient Expansion for Exchange in Solids and Surfaces. *Phys. Rev. Lett.* **2008**, *100*, 136406.

(38) Tkatchenko, A.; Scheffler, M. Accurate Molecular Van Der Waals Interactions from Ground-State Electron Density and Free-Atom Reference Data. *Phys. Rev. Lett.* **2009**, *102*, 073005.

(39) Blöchl, P. E. Projector Augmented- Wave Method. *Phys. Rev. B* **1994**, *50*, 17953–17979.

(40) Kresse, G.; Hafner, J. Ab Initio Molecular-Dynamics Simulation of the Liquid-Metal–Amorphous-Semiconductor Transition in Germanium. *Phys. Rev. B* **1994**, *49*, 14251–14269.

(41) Kresse, G.; Furthmüller, J. Efficient Iterative Schemes for Ab Initio Total-Energy Calculations Using a Plane-Wave Basis Set. *Phys. Rev. B - Condens. Matter Mater. Phys.* **1996**, *54*, 11169–11186.

(42) Kresse, G.; Furthmüller, J. Efficiency of Ab-Initio Total Energy Calculations for Metals and Semiconductors Using a Plane-Wave Basis Set. *Comput. Mater. Sci.* **1996**, *6*, 15–50.

(43) Kresse, G.; Hafner, J. Ab Initio Molecular Dynamics for Liquid Metals. *Phys. Rev. B* **1993**, *47*, 558–561.

(44) Butler, K. T.; Hendon, C. H.; Walsh, A. Electronic Chemical Potentials of Porous Metal-Organic Frameworks. *J. Am. Chem. Soc.* **2014**, *136*, 2703–2706.

(45) GitHub - WMD-group/MacroDensity: Analyse VASP density & potential grids using python https://github.com/WMD-group/MacroDensity (accessed Mar 15, 2020).

(46) Tang, W.; Sanville, E.; Henkelman, G. A Grid-Based Bader Analysis Algorithm without Lattice Bias. *J. Phys. Condens. Matter* **2009**, *21*.

(47) Henkelman, G.; Arnaldsson, A.; Jónsson, H. A Fast and Robust Algorithm for Bader Decomposition of Charge Density. *Comput. Mater. Sci.* **2006**, *36*, 354–360.

(48) Yu, M.; Trinkle, D. R. Accurate and Efficient Algorithm for Bader Charge Integration. *J. Chem. Phys.* **2011**, *134*, 064111.

(49) Zeppenfeld, A. C.; Fiddler, S. L.; Ham, W. K.; Klopfenstein, B. J.; Page, C. J. Variation of Layer Spacing in Self-Assembled Hafnium-1,10-Decanediylbis(Phosphonate) Multilayers As Determined by Ellipsometry and Grazing Angle X-Ray Diffraction. *J. Am. Chem. Soc.* **1994**, *116*, 9158–9165.

(50) Moore, D. B.; Beekman, M.; Zschack, P.; Johnson, D. C. Synthesis of Four New Members of the $(PbSe)_{1.16}(TiSe_2)_n$ (n = 1, 2, 3, and 4) Family of Ferecrystals. In *2011 11th IEEE International Conference on Nanotechnology*; IEEE, 2011; pp 1363–1366.

(51) Bauers, S. R.; Merrill, D. R.; Moore, D. B.; Johnson, D. C.

Carrier Dilution in $TiSe_2$ Based Intergrowth Compounds for Enhanced Thermoelectric Performance. *J. Mater. Chem. C* **2015**, *3*, 10451–10458.

(52) Bauers, S.; Ditto, J.; Moore, D. B.; Johnson, D. C. Structure-Property Relationships in Non-Epitaxial Chalcogenide Heterostructures: The Role of Interface Density on Charge Exchange. *Nanoscale* **2016**, *8*, 14665–14672.

(53) Reshak, A. H.; Auluck, S. Electronic and Optical Properties of the 1 T Phases of TiS_2, $TiSe_2$, and $TiTe_2$. *Phys. Rev. B* **2003**, *68*, 245113.

(54) Wiedemeier, H.; von Schnering, H. G. Refinement of the Structures of GeS, GeSe, SnS and SnSe. *Zeitschrift für Krist.* **1978**, *148*, 295–303.

(55) Beekman, M.; Cogburn, G.; Heideman, C.; Rouvimov, S.; Zschack, P.; Neumann, W.; Johnson, D. C. New Layered Intergrowths in the Sn-Mo-Se System. *J. Electron. Mater.* **2012**, *41*, 1476–1480.

(56) Alemayehu, M. B.; Falmbigl, M.; Ta, K.; Grosse, C.; Westover, R. D.; Bauers, S. R.; Fischer, S. F.; Johnson, D. C. Structural and Electrical Properties of $([SnSe]_{1+\delta})_M(NbSe_2)_1$ Compounds: Single $NbSe_2$ Layers Separated by Increasing Thickness of SnSe. *Chem. Mater.* **2015**, *27*, 867–875.

(57) Atkins, R.; Dolgos, M.; Fiedler, A.; Grosse, C.; Fischer, S. F.; Rudin, S. P.; Johnson, D. C. Synthesis and Systematic Trends in Structure and Electrical Properties of $[(SnSe)_{1.15}]_m(VSe_2)_1$, m = 1, 2, 3, and 4. *Chem. Mater.* **2014**, *26*, 2862–2872.

(58) Lygo, A. C.; Hamann, D. M.; Moore, D. B.; Merrill, D. R.; Ditto, J.; Esters, M.; Orlowicz, J.; Wood, S. R.; Johnson, D. C. Kinetically Controlled Formation and Decomposition of Metastable $[(BiSe)_{1+\delta}]_m[TiSe_2]_m$ Compounds. *J. Am. Chem. Soc.* **2018**, *140*, 3385–3393.

(59) Wood, S. R.; Merrill, D. R.; Mitchson, G.; Lygo, A. C.; Bauers, S. R.; Hamann, D. M.; Sutherland, D. R.; Ditto, J.; Johnson, D. C. Modulation Doping in Metastable Heterostructures via Kinetically Controlled Substitution. *Chem. Mater.* **2017**, *29*, 773–779.

(60) Moore, D. B.; Stolt, M. J.; Atkins, R.; Sitts, L.; Jones, Z.; Disch, S.; Beekman, M.; Johnson, D. C. Structural and Electrical Properties of $(PbSe)_{1.16}TiSe_2$. *Emerg. Mater. Res.* **2012**, *1*, 292–298.

(61) Moore, D. B.; Beekman, M.; Disch, S.; Zschack, P.; Häusler, I.; Neumann, W.; Johnson, D. C. Synthesis, Structure, and Properties of Turbostratically Disordered $(PbSe)_{1.18}(TiSe_2)_2$. *Chem. Mater.* **2013**, *25*, 2404–2409.

(62) Wood, S. R.; Merrill, D. R.; Falmbigl, M.; Moore, D. B.; Ditto, J.; Esters, M.; Johnson, D. C. Tuning Electrical Properties through Control of $TiSe_2$ Thickness in $(BiSe)_{1+\delta}(TiSe_2)_N$ Compounds. *Chem. Mater.* **2015**, *27*, 6067–6076.

(63) Merrill, D. R.; Sutherland, D. R.; Ditto, J.; Bauers, S. R.; Falmbigl, M.; Medlin, D. L.; Johnson, D. C. Kinetically Controlled Site-Specific Substitutions in Higher-Order Heterostructures. *Chem. Mater.* **2015**, *27*, 4066–4072.

(64) Falmbigl, M.; Alemayehu, M. B.; Merrill, D. R.; Beekman, M.; Johnson, D. C. In-Plane Structure of Ferecrystalline Compounds. *Cryst. Res. Technol.* **2015**, *50*, 464–472.

(65) Göhler, F.; Hamann, D. M.; Rösch, N.; Wolff, S.; Logan, J. T.; Fischer, R.; Speck, F.; Johnson, D. C.; Seyller, T. Electronic Structure of Designed $[(SnSe)_{1+\delta}]_m[TiSe_2]_2$ Heterostructure Thin Films with Tunable Layering Sequence. *J. Mater. Res.* **2019**, *34*, 1965–1975.

(66) Bauers, S. R.; Johnson, D. C. Designing Thermoelectric Materials Using 2D Layers. In *Handbook of Solid State Chemistry*; Wiley-VCH Verlag GmbH & Co. KGaA, 2017; pp 93–122.

(67) Sheets, W. C.; Mercey, B.; Prellier, W. Effect of Charge Modulation in $(LaVO_3)_m(SrVO_3)_n$ Superlattices on the Insulator-Metal Transition. *Appl. Phys. Lett.* **2007**, *91*.

(68) Miyasaka, S.; Okuda, T.; Tokura, Y. Critical Behavior of Metal-Insulator Transition in $La_{1-X}Sr_xVO_3$. *Phys. Rev. Lett.* **2000**, *85*, 5388–5391.

(69) Zubair Ansari, M.; Khare, N. Thermally Activated Band Conduction and Variable Range Hopping Conduction in Cu_2ZnSnS_4 thin Films. *J. Appl. Phys.* **2015**, *117*.

(70) Huang, Y. L.; Chiu, S. P.; Zhu, Z. X.; Li, Z. Q.; Lin, J. J. Variable-Range-Hopping Conduction Processes in Oxygen Deficient Polycrystalline ZnO Films. In *Journal of Applied Physics*; 2010; Vol. 107.

(71) Khan, M. H.; Pal, S. Nature of Electrical Hopping Conduction and Magnetotransport Studies in the Electron Doped Manganite $Ca_{0.85}Gd_{0.15}MnO_3$. *Phys. Lett. Sect. A Gen. At. Solid State Phys.* **2015**, *379*, 401–406.

(72) Hill, R. M. Variable□range Hopping. *Phys. status solidi* **1976**, *34*, 601–613.

(73) Edwards, P. P.; Sienko, M. J. The Transition to the Metallic State. *Acc. Chem. Res.* **1982**, *15*, 87–93.

(74) Möbius, A. The Metal-Insulator Transition in Disordered Solids: How Theoretical Prejudices Influence Its Characterization A Critical Review of Analyses of Experimental Data. *Critical Reviews in Solid State and Materials Sciences*. Taylor and Francis Inc. January 2019, pp 1–55.

(75) Wang, Y.; Nakano, M.; Kashiwabara, Y.; Matsuoka, H.; Iwasa, Y. Transport Properties of a Few Nanometer-Thick $TiSe_2$ Films Grown by Molecular-Beam Epitaxy. *Appl. Phys. Lett.* **2018**, *113*, 073101.

(76) Watson, M. D.; Beales, A. M.; King, P. D. C. On the Origin of the Anomalous Peak in the Resistivity of $TiSe_2$. *Phys. Rev. B* **2019**, *99*.

(77) Di Salvo, F. J.; Moncton, D. E.; Waszczak, J. V. Electronic Properties and Superlattice Formation in Semimetal $TiSe_2$. *Phys. Rev. B* **1976**, *14*, 4321.

(78) Kehoe, A. B.; Scanlon, D. O.; Watson, G. W. Nature of the Band Gap of Tl_2O_3. *Phys. Rev. B - Condens. Matter Mater. Phys.* **2011**, *83*, 233202.

(79) Monney, C.; Battaglia, C.; Cercellier, H.; Aebi, P.; Beck, H. Exciton Condensation Driving the Periodic Lattice Distortion of 1T-$TiSe_2$. *Phys. Rev. Lett.* **2011**, *106*, 106404.

(80) Bianco, R.; Calandra, M.; Mauri, F. Electronic and Vibrational Properties of $TiSe_2$ in the Charge-Density-Wave Phase from First Principles. *Phys. Rev. B - Condens. Matter Mater. Phys.* **2015**, *92*, 094107.

(81) Cazzaniga, M.; Cercellier, H.; Holzmann, M.; Monney, C.; Aebi, P.; Onida, G.; Olevano, V. Ab Initio Many-Body Effects in $TiSe_2$: A Possible Excitonic Insulator Scenario from GW Band-Shape Renormalization. *Phys. Rev. B - Condens. Matter Mater. Phys.* **2012**, *85*, 195111.

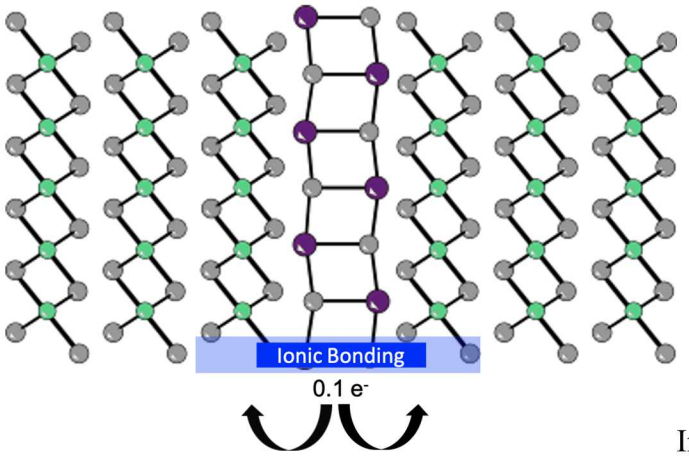

Insert Table of Contents artwork here